On the Role of Electron Precipitation in Excess Radiation Doses Measured at Aviation Altitudes

Julia Luna Claxton[1], **Robert Marshall**[1]

[1]Ann and H. J. Smead Department of Aerospace Engineering Sciences, University of Colorado Boulder
[1]Boulder, CO, USA

Key Points:

- An existing model of particle precipitation is used to predict radiation dose rates due to galactic cosmic rays (GCRs) and relativistic electron precipitation (REP).
- Our predictions of GCR dose rates are in statistical agreement with aircraft dosimetry data, but do not explain a small population of higher dose rates.
- We model REP-induced dose rates and find that they are unlikely to account for the difference between GCR modeling and aircraft dosimetry data.

Corresponding author: Julia Luna Claxton, `julia.claxton@colorado.edu`

Abstract

Radiation from space in the form of galactic cosmic rays (GCRs) generates a persistent background of ionizing radiation in Earth's atmosphere. The dose rate of ionizing radiation due to GCRs increases from sea level to aviation altitudes. The Nowcast of Aerospace Ionizing RAdiation System (NAIRAS) model is the state-of-the-art model for predicting radiation dose rates at aviation altitudes and is used to limit doses to aircrew and passengers. However, dosimetry data from the Automated Radiation Measurements for Aerospace Safety (ARMAS) system flown on commercial aircraft have revealed dose rates at aviation altitudes greater than predicted by NAIRAS. One theory, supported by correlation analyses, posits that these so-called excess dose rates are caused by relativistic electron precipitation (REP) driven by hiss waves in the inner magnetosphere. In this work, we use a validated Monte Carlo model of particle transport through the atmosphere in combination with GCR measurements from low Earth orbit (LEO) to attempt to explain the ARMAS dose rate measurements with GCRs alone. We find that our predicted GCR dose rates are in statistical agreement with the ARMAS data, but still underestimate the dose rates for some events. We then simulate REP using electron measurements from LEO and find that REP can only explain up to about 3% of the difference between GCR dose rates and ARMAS data in the most extreme cases. With support from previous literature, we conclude that REP is unlikely to be the source of the discrepancies between GCR dose rate predictions and ARMAS measurements.

Plain Language Summary

Background radiation levels are higher in aircraft than they are on the ground due to their proximity to space. The airline industry relies on advanced computer simulations to predict high-altitude radiation levels to limit radiation doses to aircrew and passengers. However, measurements of radiation taken on airplanes have revealed occasional radiation spikes that these simulations did not predict. The reason for these spikes is currently unknown. One leading theory says that the spikes could be caused by a well-known process where natural radio waves in space divert extra radiation from space to Earth. In this paper, we test that theory using our own computer simulation and data from radiation detectors in space. We find that radiation sent into Earth's atmosphere by radio waves is unlikely to be the reason for the spikes and that further investigation is required to determine why our radiation predictions do not match the aircraft measurements.

1 Introduction

Relativistic charged particles from space are a major source of radiation on Earth. These particles collide with the atmosphere and create showers of secondary particles that can propagate down to tens of kilometers above sea level and even reach the ground. Exposure to these energetic particles and their secondary showers can ionize human tissue. Lifetime exposure to ionizing radiation in conjunction with peak dose rate is a major predictive factor in the development of cancerous and non-cancerous adverse health effects (Lowe et al., 2022; Shah et al., 2014). At commercial aviation altitudes (approximately 8 to 11 km above sea level), ionizing radiation doses from spaceborne particles are elevated compared to sea level due to a reduction in atmospheric shielding of these particles. Therefore, frequent fliers and aircrew are exposed to higher lifetime radiation exposure and peak dose rates than people on the ground. We thus require accurate models of radiation dose rates as a function of altitude to limit radiation doses to aircrew and passengers and ensure human safety. The industry standard for modeling ionizing radiation dose rates at aviation altitudes is the Nowcast of Aerospace Ionizing RAdiation System (NAIRAS) model maintained by NASA (Mertens et al., 2013). NAIRAS predicts background radiation doses due to galactic cosmic rays (GCRs) and solar energetic particles (SEPs).

The Automated Radiation Measurements for Aerospace Safety (ARMAS) system is a set of dosimeters that have been flown in the last decade on commercial aircraft to monitor the radiation environment at aviation altitudes (Tobiska et al., 2016). Data from the ARMAS system has revealed sporadic dose rate spikes at aviation altitudes, sometimes in excess of two times the NAIRAS-predicted dose rate (Tobiska et al., 2016, 2018). The cause of these excess doses is unknown, and a number of theories have emerged to explain them. One theory posits that relativistic electron precipitation (REP) may cause these excess doses. While energetic electrons cannot reach aviation altitudes, their secondary particles can, in particular X-rays and gamma rays produced by bremsstrahlung in the atmosphere. This theory is supported by correlation analyses (Aryan et al., 2023; Aryan, Bortnik, Tobiska, Mehta, Siddalingappa, & Hogan, 2025; Aryan, Bortnik, Tobiska, Mehta, Hogan, & Challa, 2025), but has not yet been physically modeled to constrain the potential contribution of electron precipitation to excess dose rates.

In this work, we use energetic electron data collected from low Earth orbit (LEO) in combination with a validated particle precipitation model to quantify the contribution of electron precipitation to radiation dose rates at aviation altitudes. First, we use galactic cosmic ray (GCR) data measured in LEO in combination with a validated model of energetic particle precipitation to attempt to explain the ARMAS dose rates with GCRs alone. We then compare our model estimates to ARMAS data and identify cases of excess dose rates. Next, we forward model precipitating electron fluxes measured from LEO through the atmosphere to predict the radiation dose rate caused by radiation belt electron precipitation. We then compare the electron-induced dose rate to the excess dose rates between our GCR modeling and ARMAS. We find that REP-induced dose rates are unlikely to explain the excess dose rates, in agreement with previous literature.

2 Background

There are two well-known sources of background radiation doses at aviation altitudes: SEPs and GCRs (Mertens et al., 2013). The state-of-the-art model for predicting radiation doses across the Earth's atmosphere, NAIRAS (Mertens et al., 2013), accounts for both of these radiation types. NAIRAS parameterizes incoming GCR spectra using high-latitude neutron counts. Neutrons are produced as a cascade product from GCRs incident on the atmosphere, and thus their detection rate at the ground serves as an indirect measure of GCR incidence. NAIRAS then propagates the derived GCR spectrum through the heliosphere, magnetosphere, and atmosphere to produce dose rate predictions. We do not discuss SEP contributions to dose rate in this paper, as there are no ARMAS data records correlated with SEP events. NAIRAS, currently in version 3, was validated with aircraft dosimeter data from the RAD-X balloon campaign showing agreement within the measurement uncertainty of $\pm 30\%$. In this work, we utilize NAIRAS version 3 values that are provided with ARMAS data.

Tobiska et al. (2016) reported measurements from the ARMAS system revealing unexpected dose rate spikes at aviation altitudes, in some cases doubling NAIRAS version 2 predictions. These elevated dose rates were observed between L-shells of 1.5 and 5. This L-shell range led the authors to speculate that the dose rate spikes could be caused by relativistic electron precipitation (REP) driven by electromagnetic ion-cyclotron (EMIC) waves in the outer radiation belt. In Tobiska et al. (2018), the excess dose rates recorded by ARMAS were posited to be caused by secondary bremsstrahlung X-rays generated by relativistic electron precipitation, and the ARMAS database was released publicly for further investigation.

If these excess dose rates are caused by electron precipitation from the radiation belts, then one would expect to find a correlation between excess dose rates and well-known drivers of REP. This led to a number of correlation studies investigating the idea that the excess dose rates could be caused by REP. In the first of these studies, Aryan et al. (2023) conducted a correlation analysis between excess dose rates and magnetospheric wave power during magnetic conjunctions between the Van Allen Probes and ARMAS (ΔL $<$ 1, ΔMLT $<$ 1 hr). They parameterized wave power by the power spectral density (PSD) in characteristic frequency bands for EMIC, hiss, chorus, and generalized high-frequency waves. They found a correlation between PSD in a frequency band associated with hiss (100 Hz to 2 kHz) and excess dose rate, as well as a weaker correlation between PSD in a chorus-associated band (0.1x to 1x the electron gyrofrequency) and excess dose rate. They concluded that hiss-driven precipitation may play a significant role in the generation of excess dose rates.

Continuing this work, Aryan, Bortnik, Tobiska, Mehta, Siddalingappa, and Hogan (2025) and Aryan, Bortnik, Tobiska, Mehta, Hogan, and Challa (2025) performed cross-correlation studies showing that the correlation between hiss-associated PSD and excess dose rate is strongest for close conjunctions in L-shell and magnetic local time (MLT) and decreases with increasing conjunction distance and time. Furthermore, they found a less rapid dropoff in correlation coefficient for eastward changes in MLT compared to westward changes, consistent with electron drift. However, their sampling distribution was heavily biased towards the post-noon and pre-midnight MLT sectors where hiss waves are primarily observed (Dong et al., 2024; Hartley et al., 2018; Li et al., 2015), with a total of only 7 datapoints in the 0000 to 0600 sector. They concluded that the excess dose rates measured by ARMAS were most likely caused by hiss-driven electron precipitation.

Despite the growing body of correlation studies between drivers of electron precipitation and excess dose rate, few modeling studies have been performed to quantitatively constrain the dose rates that electron precipitation could induce at aviation altitudes. Xu et al. (2021) studied the dose rates induced by monoenergetic beams of electrons propagated through a simulated atmosphere using the Energetic Precipitation Monte Carlo (EPMC) model (Lehtinen et al., 1999) in conjunction with the Monte Carlo model for Photons (MCP) (Xu et al., 2012). They predicted that a precipitating flux of 10^8 electrons $\cdot$ m^{-2} $\cdot$ s^{-1} of 10 MeV electrons would induce a dose rate of just over 0.1 μSv/hr at 11 km. The quality factor converting Gy to Sv in silicon is approximately 2, meaning they predicted an induced dose rate of approximately 0.05 μGy/hr in a silicon detector at aviation altitudes. They also predicted that precipitating electrons with energies less than $\sim$ 1 MeV do not meaningfully contribute to dose rates at aviation altitudes. However, their work did not model realistic energy distributions of energetic electrons, instead reporting the induced dose rates for single monoenergetic beams.

McMurchie (2022) used the Xu et al. (2021) parameterization of REP-induced dose rates to predict dose rates due to precipitating electron spectra derived from the POES constellation. They conducted three case studies corresponding to storm time, moderate disturbance, and quiet time. They predicted that electron precipitation explained up to 0.035% of the total (not excess) ARMAS-measured dose rate during the storm case, 3.66% of the total dose rate in the moderate disturbance case, and 0.015% of the total dose rate in the quiet case. However, the precipitating electron spectra that they used in their modeling were limited due to the coarse energy resolution of the POES detectors, the limited coverage of high-energy electrons in those detectors, and contamination between the 0° and 90° telescopes (Selesnick et al., 2020).

In this work, we use a validated Monte Carlo model in conjunction with the highest-quality measurements of precipitating electrons currently available to quantitatively constrain the contribution of electron precipitation to the unexplained excess dose rates measured by ARMAS. To our knowledge, this is the first study to directly compare simulated dose rates using high-quality in-situ measurements of precipitating particles (including protons, alpha particles, and electrons) to the excess dose rates recorded by ARMAS. This work is thus the most direct evaluation to date of the hypothesis that REP is responsible for the ARMAS excess dose rates.

3 Model Description: WASPP

In this work, we utilize the Whole Atmosphere Simulation of Particle Precipitation (WASPP) model. WASPP is a modification of the model introduced in Berland et al. (2023). WASPP utilizes the Geant4 simulation package developed by CERN (Agostinelli et al., 2003) to simulate a 1000 km MSIS atmosphere divided into 1 km slabs. Particles of arbitrary species, energy, and direction can be injected at any point in the simulated atmosphere and traced through their lifetime. WASPP accounts for secondary cascade processes, including electron production via ionization, photoelectron production, and pair production, as well as pair annihilation, bremsstrahlung photon production, and Compton scattering (Berland et al., 2023). Note that this is not an exhaustive list of processes included in the WASPP model. For more information, see the Geant4 documentation describing the QBBC physics list (Geant4 Collaboration, 2023). WASPP-simulated electron backscatter has been validated using data from low Earth orbit in Claxton and Marshall (2026). WASPP features a 3-dimensional vector dipolar magnetic field model, providing magnetic mirroring without the use of a nonphysical external mirroring force. For this work, we configured WASPP to operate at a magnetic latitude of 45°, corresponding roughly to the magnetic latitude of the continental United States where the majority of ARMAS data were recorded. The magnetic dip angle at this latitude at an altitude of 450 km in our simulation is 26.6° from vertical-down.

3.1 Simulated Dose Rate Calculation

We begin by attempting to explain the ARMAS dose rate measurements using an upper-bound estimate of GCR-induced dose rates. In addition to validating the WASPP model, these simulations provide a picture of data-driven dose rates produced by GCRs and their day-to-day variability based on direct measurements from LEO.

To model the dose rate induced by GCRs at aviation altitudes, we needed to calculate the dose rate induced by a given set of precipitating particles. For protons, electrons, and alpha particles, we utilized the fact that particle flux multiplied by stopping power in a material of interest (e.g. silicon) yields a dose rate in that material. The cumulative dose rate induced by protons, electrons, and alpha particles at altitude h is given by

$$\mathrm{DR}_{\mathrm{p}^+,\mathrm{e}^-,\alpha}(h) = \sum_i \sum_E \Phi_i(E,h) \cdot \mathrm{S}_i(E,h), \tag{1}$$

where i represents particle species, E is the energy of an incident particle, $\Phi_i(E)$ is the flux of species i at energy E, S is the stopping power of silicon for species i at energy E, and $\mathrm{DR}_{\mathrm{p}^+,\mathrm{e}^-,\alpha}$ is the resultant cumulative dose rate in silicon due to these particles.

High-energy photons are another important source of ionizing radiation doses. Since stopping power is not defined for photons, we estimated the energy deposited in a silicon detector by photons using the X-ray mass energy-absorption coefficient μ_{en}. For a given photon, μ_{en} multiplied by the incident photon energy yields the net energy deposition in a target material per unit flux accounting for both energy deposition by the original photon and energy losses via re-radiation of secondaries. Multiplying by a photon flux thus yields the dose rate in silicon due to photons. Thus, for a given flux of photons Φ_γ, the photon contribution to dose rate (DR_γ) is

$$\mathrm{DR}_\gamma(h) = \sum_E \Phi_\gamma(E,h) \cdot E \cdot \mu_{\mathrm{en}}(E), \tag{2}$$

and the total dose rate (DR) is

$$\mathrm{DR}(h) = \mathrm{DR}_{\mathrm{p}^+,\mathrm{e}^-,\alpha}(h) + \mathrm{DR}_\gamma(h). \tag{3}$$

Stopping power tables were sourced from NIST for protons (1 keV to 10 GeV), electrons (10 keV to 1 GeV), and alphas (1 keV to 1 GeV) (Berger et al., 2009). X-ray mass energy-absorption coefficients were sourced from NIST for photons between 1 keV and 20 MeV (Hubbell & Seltzer, 2004). The value of μ_{en} for photons above 20 MeV was taken as the value at 20 MeV, as μ_{en} does not change significantly with energy above $\sim$ 5 MeV in the NIST database. This extrapolation added approximately 1.6 μGy/hr to our predicted GCR dose rates. Stopping power and X-ray mass energy-absorption coefficient as a function of energy are shown in Figure 1.

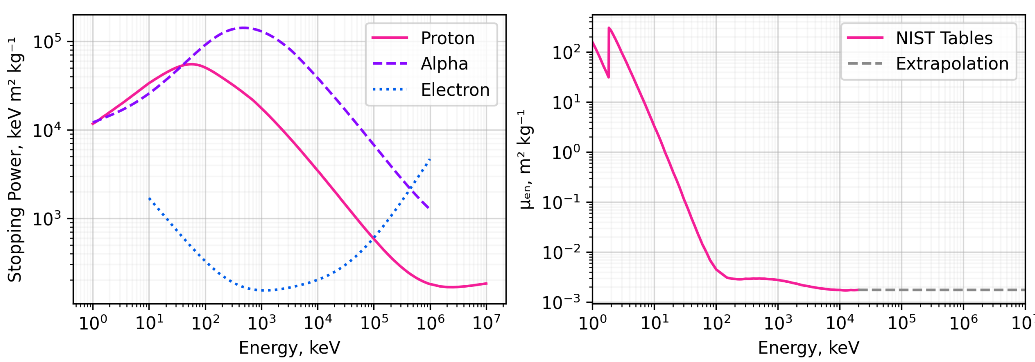

Figure 1. Stopping power (left) and X-ray mass energy-absorption coefficient (right) as a function of energy sourced from NIST databases.

Since the calculation of dose rate is species- and energy-dependent, we need to record an energy spectrum for every species of interest at every location where we want to calculate a dose rate in our simulation. Since we are interested in the altitude profile of EPP-induced dose rates, we configure WASPP to record the energy spectrum of all electrons, protons, alphas, and photons passing through a set of recording altitudes. These recording altitudes are spaced from sea level to 100 km altitude in 1 km increments. After a simulation run is completed, the counts recorded in every energy bin at each recording altitude are divided by the total number of input particles. This division produces a normalized response table giving the number of counts of a given particle that are produced by one precipitating primary particle over the energies and altitudes of interest. An example of these normalized response spectra is shown in Figure 2. The spectra shown are the response to a monoenergetic input beam of 10^5 protons each with an energy of 1.0 GeV injected into the simulation at 449.5 km with an initial velocity randomly sampled from an isotropically downgoing distribution. Secondary alpha fluxes are negligible and are not shown in the figure. The primary protons are evident as the white line in the leftmost panel, with the primary energy decreasing at low altitudes. The 511 keV photon line due to pair annihilation is evident in the rightmost panel.

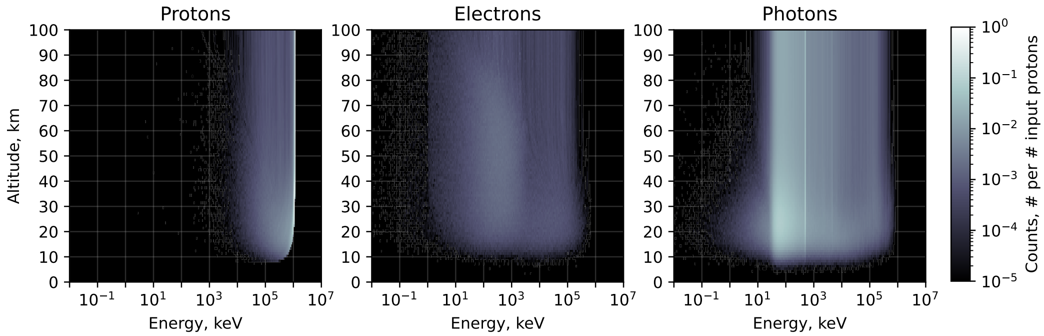

Figure 2. Example simulated energy spectra as a function of altitude for protons (left), electrons (center), and photons (right). These spectra are the response to an input beam of 10^5 protons at 1.0 GeV injected with isotropic downgoing incidence into an MSIS atmosphere at 449.5 km.

4 Galactic Cosmic Ray Dose Rates

While the primary goal of this study is to constrain dose rates due to REP, we first attempt to explain the ARMAS-measured dose rates with GCRs alone. Since NAIRAS estimates of GCR dose rates do not explain the ARMAS dose rates, we seek to model upper-bound GCR dose rates using our own modeling. To perform this modeling, we utilize data from the Alpha Magnetic Spectrometer (AMS-02) on board the International Space Station (ISS) (Cadoux et al., 2002). AMS-02 measures GCR energy spectra at a daily cadence for a number of particle species. In this work, we consider the proton and alpha particle contribution to dose rate. AMS-02 measures GCR protons between 0.4 GeV and 99 GeV and alpha particles between 1.3 GeV and 135.7 GeV.

To convert a spectrum measured by AMS-02 into a dose rate profile, we used the WASPP model to inject a series of monoenergetic proton and alpha beams into a simulated atmosphere. Each beam had an energy corresponding to the mean energy of an AMS-02 energy channel. We injected these beams into our simulation with an initial velocity randomly selected from an isotropically downgoing distribution. Each beam consisted of 10^5 particles. As described in Section 3.1, energy spectra of primary particles and cascade products were recorded along the atmospheric column for each beam. These spectra provide a basis set of atmospheric responses to protons and alpha particles. The response tables were saved to a datafile for later lookup. Performing a sum of these lookup tables weighted by the flux measured by AMS-02 thus provides a composite atmospheric response for a given AMS-02 spectrum.

To calculate lookup table weights, we first integrate a given AMS-02 spectrum over solid angle. This solid angle integration is performed over a full 2π hemisphere, thus assuming an isotropic distribution of incoming GCRs. In reality, the solid angle over which GCRs arrive at LEO is rigidity-dependent and smaller than 2π for particles with rigidities below approximately 10 GV (Chen et al., 2025). The isotropic hemisphere assumption likely overestimates the flux of lower-rigidity particles, thus increasing our GCR dose rate predictions. This assumption was made for ease of calculation and in pursuit of our goal of finding an upper-bound GCR dose rate.

After solid angle integration, we perform a trapezoidal integration over energy with bounds corresponding to the midpoints between the beam energies we injected into the WASPP simulation. This step produces a flux in units of particles $\cdot$ $\mathrm{m}^{-2}\ \mathrm{s}^{-1}$. The atmospheric response table corresponding to each beam was then multiplied by the integrated flux derived from AMS-02 for that beam. The response due to each beam is then summed for every species, creating composite energy spectra at every 1-kilometer altitude step between 0 km and 100 km above sea level. The resulting dose rate is then derived from these spectra following the process described in Section 3.1. An example spectrum recorded by AMS-02 and the associated dose rate calculated from our model are shown in Figure 3. The dose rate includes the contributions of protons and alpha particles.

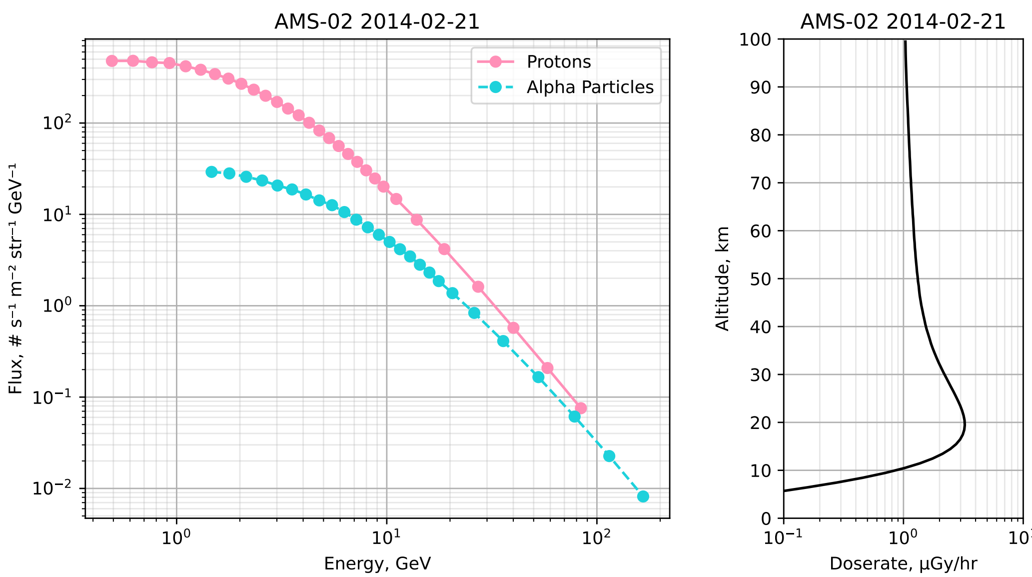

Figure 3. Left: Example of a cosmic ray spectrum measured in low Earth orbit by AMS-02 for protons (solid pink line) and alpha particles (dashed blue line). Right: Dose rate in silicon as a function of altitude predicted by our model due to the AMS-02-measured spectrum.

In Figure 4, we plot four example conjunctions showing a) agreement between WASPP, NAIRAS, and ARMAS; b) disagreement between NAIRAS and ARMAS, but agreement between ARMAS and WASPP; c) small excess dose rates in ARMAS above the WASPP prediction; and d) large excess dose rates in ARMAS above the WASPP prediction. Error bars on ARMAS data represent the 1σ uncertainty, which is 20%. WASPP predictions of dose rate are derived from AMS-02 data recorded on the date of each panel. Note that AMS-02 data is provided at a daily cadence for the ISS's orbit at 51° inclination, spanning a range of latitudes, while the ARMAS data is primarily limited to the mid-latitudes of the continental United States. Thus, the AMS-02 data experiences a wider range of cutoff rigidities than ARMAS and may record higher fluxes at low rigidities than ARMAS would experience, causing another potential overestimation of GCR dose rates. Once again, we accept this overestimation in order to determine if the excess dose rates can be explained by an upper-bound case for GCR dose rates.

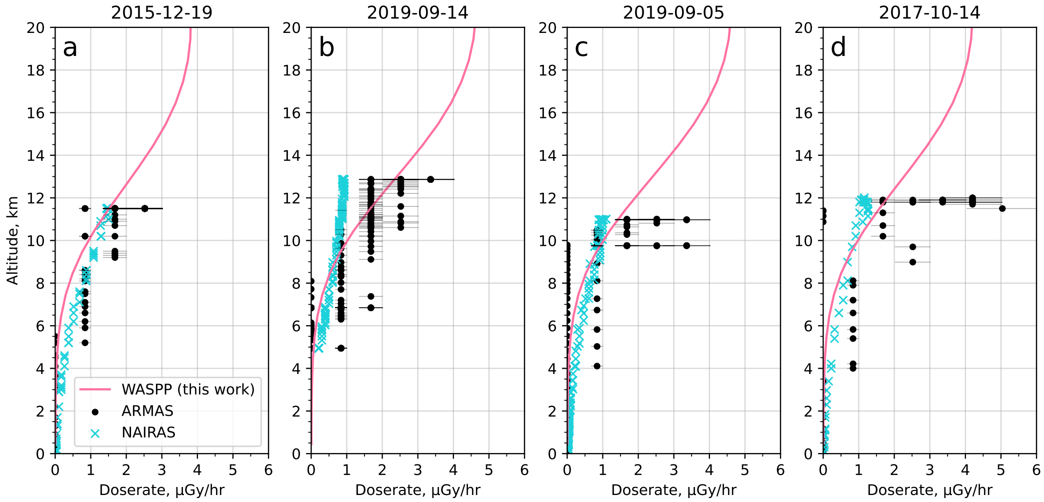

Figure 4. Four example conjunction dates between ARMAS and AMS-02 showing the ARMAS-measured dose rate (black dots), NAIRAS-predicted GCR dose rate (blue crosses), and our predicted GCR dose rate based on AMS-02 data (pink line).

With the ability to compute a dose rate profile from an AMS-02 spectrum, we next compare our predicted GCR dose rates to ARMAS-measured dose rates for every day where AMS-02 and ARMAS both recorded data. For each day, we subtract our predicted GCR-induced dose rate from the ARMAS-measured dose rate to produce a residual dose rate. The GCR-induced dose rate was taken at the same altitude of each ARMAS data record. The results of this comparison are shown in Figure 5, along with the results of the same procedure using NAIRAS version 3 predictions of GCR dose rate for reference.

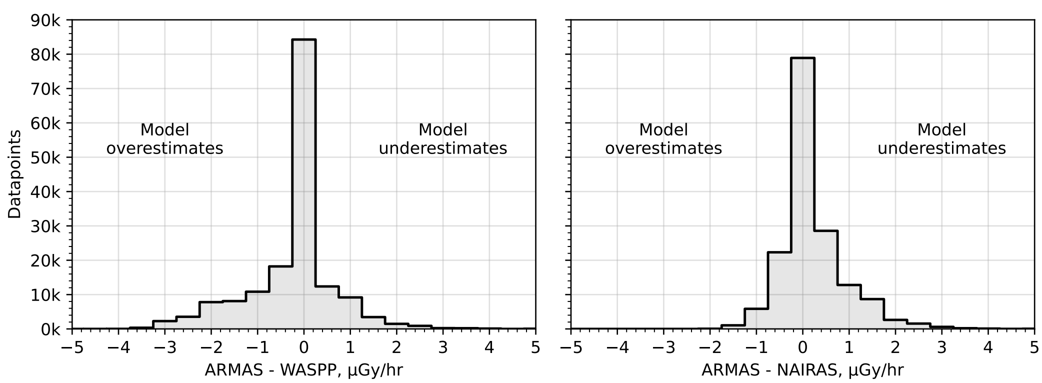

Figure 5. Left: Residuals between our GCR dose rate predictions and ARMAS data for all conjunction dates with AMS-02. Right: Residuals between NAIRAS predictions and ARMAS data for the same set of dates.

The results in Figure 5 show that in general, our GCR dose rate estimations correctly predict the ARMAS data, with a preference to overestimating the ARMAS-measured dose rates more often than underestimating them. This tendency to overestimation indicates a systematic error consistent with our assumptions in favor of finding the upper-bound GCR dose rate. However, we note that the 3σ uncertainty of ARMAS is on the order of ± 1.5 μGy/hr at aviation cruising altitudes (Figure 4). Thus, some of these overestimate cases may be explained by uncertainty in the ARMAS measurements. However, there is a noticeable tail where we still underestimated the measured dose rates by up to 3 μGy/hr, despite our assumptions. Those dose rates cannot be reasonably explained by our modeling of GCRs.

Having found a subset of ARMAS dose rates measurements that we cannot explain with GCRs alone, we next investigate the potential contribution of relativistic electron precipitation to these excess dose rates.

5 Relativistic Electron Precipitation Dose Rates

To calculate the possible contribution of electron precipitation to dose rates at aviation altitudes, we require a realistic precipitating energy spectrum for energetic electrons. In this study, we use data from the Electron Losses and Fields INvestigation (ELFIN) mission (Angelopoulos et al., 2020) to provide realistic precipitating spectra. The twin ELFIN CubeSats, which flew from 2019 to 2022, measured precipitating, trapped, and backscattered electrons from low Earth orbit (450 km altitude, 93° inclination) every 2.8 seconds during its data collection periods. ELFIN measured electrons between 50 keV and 7 MeV in 16 approximately logarithmically-spaced bins. An example of ELFIN data is shown in Figure 6.

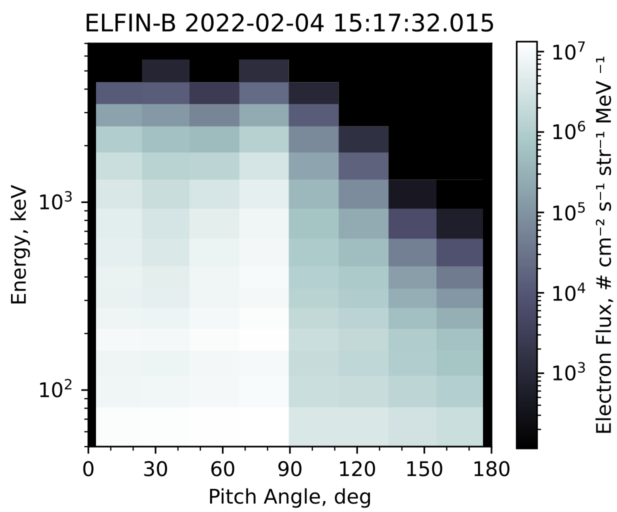

Figure 6. Example of one timestep (1.4 seconds) of ELFIN data. Data was recorded in the northern hemisphere with a loss cone angle of approximately 68°.

We aim to find precipitating electron spectra recorded by ELFIN that are most likely to explain the excess dose rates measured by ARMAS. While correlation studies between excess dose rate and electron precipitation have largely focused on hiss-driven precipitation, the energy of precipitating electrons and their production of secondary particles is the primary factor that determines their penetration depth into the atmosphere rather than a specific wave driver (Berland et al., 2023; Xu et al., 2021; Marshall & Bortnik, 2018). Therefore, harder precipitating spectra with higher fluxes above 1 MeV induce higher dose rates at aviation altitudes regardless of the wave driver of the precipitation. We therefore look for the precipitating electron spectra measured by ELFIN that had the highest fluxes of high-energy electrons to try to explain the excess dose rates. To find these spectra, we sum the precipitating flux of supra-MeV electrons (i.e. > 1 MeV) for every half-spin (corresponding to a full sweep of the electron pitch angle distribution) of each ELFIN satellite over their lifetime. We then select spectra at the 90th, 98th, and 99.9th percentile of precipitating supra-MeV fluxes for analysis. These spectra represent some of the most intense relativistic precipitation events ever recorded by the ELFIN mission. The date, time, and satellite for each spectrum is provided in Table 1, and the pitch angle-energy distribution of the 99.9th percentile REP event is shown in Figure 6.

Percentile	Date (YYYY-MM-DD)	Time (UTC)	Satellite
99.9	2022-02-04	15:17:32.015	ELFIN-B
98	2021-11-07	02:12:46.867	ELFIN-B
90	2020-10-22	23:04:22.315	ELFIN-A

Table 1. Timestamps and satellite identification information for our selected ELFIN-measured spectra.

To predict the dose rates induced by our chosen precipitating electron spectra, we injected beams of field-aligned electrons into the WASPP simulation corresponding to each of ELFIN's energy bins. The field-aligned assumption was made to reduce computation time and to maximize the penetration depth of primary electrons. The field-aligned assumption will thereby slightly overestimate the dose rate induced by electron precipitation. The resultant dose rates should thus be considered as upper bounds on the dose rate induced by each spectrum.

After injecting electron beams into WASPP, the atmospheric response of each beam is weighted by the ELFIN-measured flux at that energy using the same procedure as with AMS-02 (Section 4). The atmospheric response is then converted to a dose rate as described in Section 3.1. Our chosen REP spectra and their resulting upper-bound electron dose rates are shown in Figure 7.

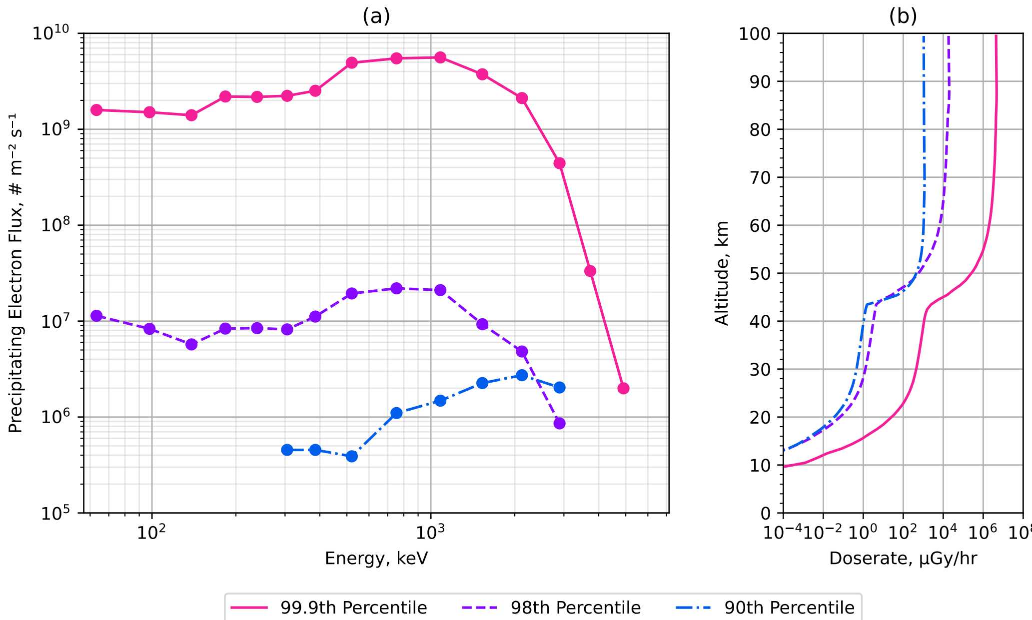

Figure 7. (a) Precipitating electron spectra derived from ELFIN-measured datapoints at the 99.9th (solid magenta line), 98th (dashed purple line), and 90th (dash-dotted blue line) percentile of supra-MeV electron precipitation events recorded by ELFIN. (b) dose rate in a silicon detector due to each of the spectra in (a) as a function of altitude.

We then compare our REP-induced dose rate to the excess dose rates we calculated in Section 4. Figure 8 shows the distribution of excess dose rates where ARMAS-measured dose rates exceeded our GCR predicted dose rates as a function of altitude. The predicted REP-induced dose rates induced by our selected events are overlaid on the same scale.

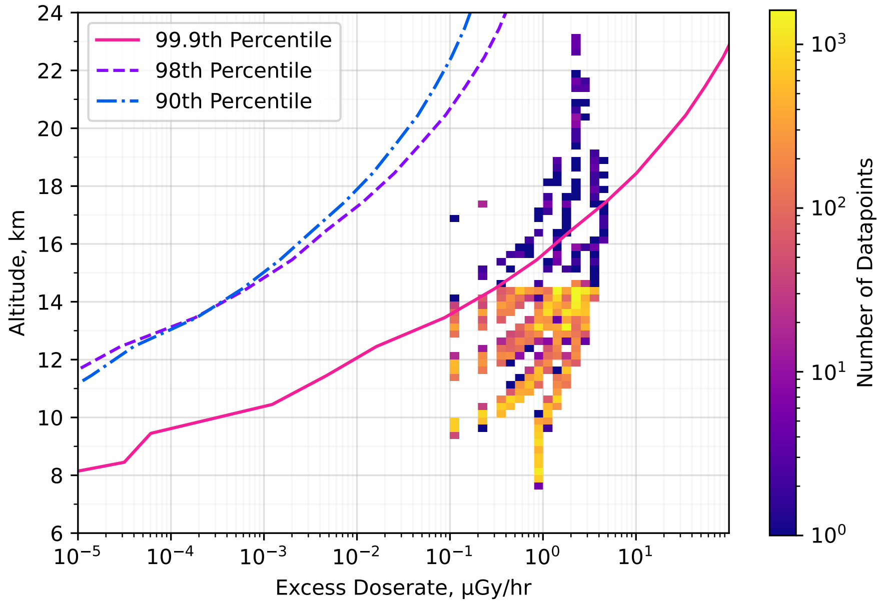

Figure 8. Distribution of excess dose rates as a function of altitude (color) with overlaid curves showing the modeled dose rate due to the 99.9th (solid magenta line), 98th (dashed purple line), and 90th (dash-dotted blue line) percentile of supra-MeV electron precipitation events recorded by ELFIN.

Figure 8 shows that the strongest relativistic electron precipitation ELFIN measured is not sufficient to explain the vast majority of excess dose rates observed by ARMAS, even with our assumptions to maximize the GCR component of total dose rate. The 99.9th percentile REP-induced dose rate can only explain 0.3% of the total number of excess dose rates recorded, and only at very high altitudes above 13 km. Meanwhile, the 98th and 90th percentile events cannot account for any of the excess dose rate measurements. Often, the REP-induced dose rates are multiple orders of magnitude smaller than the excess dose rates measured by ARMAS.

6 Discussion

At each step in our analysis where there was uncertainty in the model inputs, we made the assumption in favor of giving REP the best chance possible to explain the excess dose rates. We assumed that GCRs were isotropically incoming over one hemisphere regardless of rigidity, overestimating the dose rate contribution of GCR particles with rigidities below 10 GV. We also simulated incoming GCRs measured at lower cutoff rigidities than ARMAS experienced, allowing for potentially higher fluxes of low-rigidity particles than ARMAS would experience. Both of these assumptions increased our predicted GCR dose rates, thereby reducing the magnitude of the excess dose rates that needed to be explained by REP. Furthermore, when simulating REP, we assumed that precipitating electrons were exclusively field-aligned, maximizing their penetration depth into the atmosphere and thus their resultant dose rates. Finally, we chose to compare the excess dose rates to three cases of the most extreme REP events measured over the full lifetime of the ELFIN satellites.

However, despite these assumptions and choices, we found that the event corresponding to the 99.9th percentile of REP strength measured by ELFIN could only explain a small number of excess dose rates at high altitudes. The 98th percentile and below could not fully explain a single excess dose rate at any altitude. Furthermore, the excess dose rates explainable by the 99.9th percentile REP event only occurred above 13 km. At 11 km (a more typical aviation altitude), the dose rate due to the 99.9th percentile REP event explained only 0.1% to 3% of excess dose rate magnitudes, and the 98th and 90th percentile events explained less than 0.01% of even the smallest excess dose rate magnitude. Moreover, our modeling predicts that REP can contribute only up to approximately 0.01 μGy/hr at aviation altitudes in the most extreme cases. We thus conclude that REP cannot reasonably explain the excess dose rates measured at aviation altitudes by ARMAS.

Previous modeling efforts also support this conclusion. As previously discussed, Xu et al. (2021) predicted that a flux of 10^8 electrons $\cdot$ m^{-2} $\cdot$ s^{-1} of 10 MeV electrons, a flux orders of magnitude higher than typical observed electron fluxes at LEO, would induce a dose rate of just 0.05 μGy/hr at an altitude of 11 km. Meanwhile, typical excess dose rates are on the order of 1 μGy/hr (Figure 8). Thus, their work predicts that an extreme flux of ultrarelativistic electrons could contribute only up to about 5% of a typical excess dose rate. In the case studies presented by McMurchie (2022), the highest fraction of total (not excess) dose rate explained by REP was 3.66%. To explain the excess dose rates measured by ARMAS, REP-induced dose rates would have to make up about 10% to 50% of the total dose rate. The results of both of these studies suggest that REP is unlikely to be able to generate dose rates on the order of the observed excess dose rates.

We recognize the compelling correlation between hiss wave activity and excess dose rates presented in Aryan, Bortnik, Tobiska, Mehta, Hogan, and Challa (2025). The goal of this study is not to explain that correlation, but simply to quantitatively constrain the hypothesis that REP is responsible for that correlation. Between our analysis and previous literature, we believe it is unlikely that relativistic electron precipitation is the direct cause of the discrepancies between GCR dose rate predictions and dose rates measured by the ARMAS system.

7 Conclusion

In this work, we investigated the contribution of relativistic electron precipitation to radiation dose rates at aviation altitudes. We used the WASPP model to forward model distributions of GCR ions and radiation belt electrons measured in-situ at the top of the atmosphere to calculate radiation dose rates through a column of atmosphere. We predicted that the dose rates due to REP cannot reasonably explain excess dose rates measured at aviation altitudes. Our results are in agreement with previous literature that used a different particle transport model. We therefore conclude that radiation belt electrons are unlikely to be the source of excess radiation doses at aviation altitudes, and moreover are unlikely to contribute any noticeable dose rate at those altitudes. Further investigation is required to determine the source of these excess dose rates and the reason for their correlation with magnetospheric hiss.

Open Research Section

ELFIN data (Angelopoulos et al., 2020) is available for free at `https://data.elfin.ucla.edu/ela/`. Geant4 (Agostinelli et al., 2003) is available for free from `https://geant4.web.cern.ch/download/11.3.2.html`. The Geant4 code used to generate lookup tables is available for free at All code used to perform the analysis and generate figures is available for free at Analysis was performed using the Julia coding language (Bezanson et al., 2017), the Python coding language, NumPy (Harris et al., 2020), SpacePy (Steven K. Morley et al., 2010; Niehof et al., 2022), and Matplotlib (Hunter, 2007).

Conflict of Interest Declaration

The authors declare there are no conflicts of interest for this manuscript.

Acknowledgments

The authors acknowledge NASA award NNX14AN68G, NSF awards AGS-1242918 and AGS-2019950, and Vassilis Angelopoulos for use of ELFIN's EPD data. The authors thank Ethan Tsai for providing technical support with ELFIN data.

References

Agostinelli, S., Allison, J., Amako, K. a., Apostolakis, J., Araujo, H., Arce, P., . . . others (2003). Geant4—a simulation toolkit. *Nuclear instruments and methods in physics research section A: Accelerators, Spectrometers, Detectors and Associated Equipment*, *506*(3), 250–303.

Angelopoulos, V., Tsai, E., Bingley, L., Shaffer, C., Turner, D. L., Runov, A., . . . Zhang, G. Y. (2020, 7 30). The ELFIN Mission. *Space Science Reviews*, *216*(5), 103. Retrieved from `https://doi.org/10.1007/s11214-020-00721-7` doi: 10.1007/s11214-020-00721-7

Aryan, H., Bortnik, J., Tobiska, W. K., Mehta, P., Hogan, B., & Challa, H. (2025). Enhanced radiation at aviation altitudes and plasmaspheric hiss waves—a time shift analysis. *Journal of Geophysical Research: Space Physics*, *130*(10), e2025JA033959. Retrieved from `https://agupubs.onlinelibrary.wiley.com/doi/abs/10.1029/2025JA033959` (e2025JA033959 2025JA033959) doi: https://doi.org/10.1029/2025JA033959

Aryan, H., Bortnik, J., Tobiska, W. K., Mehta, P., & Siddalingappa, R. (2023). Enhanced radiation levels at aviation altitudes and their relationship to plasma waves in the inner magnetosphere. *Space Weather*, *21*(10), e2023SW003477. Retrieved from `https://agupubs.onlinelibrary.wiley.com/doi/abs/10.1029/2023SW003477` (e2023SW003477 2023SW003477) doi: https://doi.org/10.1029/2023SW003477

Aryan, H., Bortnik, J., Tobiska, W. K., Mehta, P., Siddalingappa, R., & Hogan, B. (2025). Cross correlation between plasmaspheric hiss waves and enhanced radiation levels at aviation altitudes. *Space Weather*, *23*(2), e2024SW004184. Retrieved from `https://agupubs.onlinelibrary.wiley.com/doi/abs/10.1029/2024SW004184` (e2024SW004184 2024SW004184) doi: https://doi.org/10.1029/2024SW004184

Berger, M., Coursey, J., & Chang, J. (2009). *Stopping-power & range tables for electrons, protons, and helium ions.* Online. National Institute of Standards and Technology Physical Measurement Laboratory. Retrieved 2025-10, from `https://www.nist.gov/pml/stopping-power-range-tables-electrons-protons-and-helium-ions` doi: https://dx.doi.org/10.18434/T4NC7P

Berland, G. D., Marshall, R. A., Capannolo, L., McCarthy, M. P., & Zheng, L. (2023). Kinetic modeling of radiation belt electrons with geant4 to study energetic particle precipitation in earth's atmosphere. *Earth and Space Science*, *10*(11), e2023EA002987. Retrieved from `https://agupubs.onlinelibrary.wiley.com/doi/abs/10.1029/2023EA002987` (e2023EA002987 2023EA002987) doi: https://doi.org/10.1029/2023EA002987

Bezanson, J., Edelman, A., Karpinski, S., & Shah, V. B. (2017). Julia: A fresh approach to numerical computing. *SIAM Review*, *59*(1), 65–98. Retrieved from `https://epubs.siam.org/doi/10.1137/141000671` doi: 10.1137/141000671

Cadoux, F., Cervelli, F., Chambert-Hermel, V., Chen, G., Chen, H., Coignet, G., . . . Zhuang, H. (2002). The ams-02 electromagnetic calorimeter. *Nuclear Physics B - Proceedings Supplements*, *113*(1), 159-165. Retrieved from `https://www.sciencedirect.com/science/article/pii/S0920563202018364` doi:

https://doi.org/10.1016/S0920-5632(02)01836-4
Chen, L., Huo, R., Li, Q., Wang, T., Xu, W., & Ye, W. (2025). Geomagfilter: Modeling the angular-rigidity joint distribution of galactic cosmic rays on low earth orbit. *Advances in Space Research*, *75*(7), 5450-5459. Retrieved from https://www.sciencedirect.com/science/article/pii/S0273117725000961 doi: https://doi.org/10.1016/j.asr.2025.01.066

Claxton, J. L., & Marshall, R. A. (2026). Electron backscatter in energetic particle precipitation: Data analysis and simulation. *Journal of Geophysical Research: Space Physics*, In publication. doi: 10.1029/2025JA034640

Dong, J., Xiang, Z., & Ni, B. (2024). On the relationship between the banded hiss distribution and plasmapause location: A survey of van allen probes observations. *Geophysical Research Letters*, *51*(22), e2024GL111893. Retrieved from https://agupubs.onlinelibrary.wiley.com/doi/abs/10.1029/2024GL111893 (e2024GL111893 2024GL111893) doi: https://doi.org/10.1029/2024GL111893

Geant4 Collaboration. (2023). *Qbbc.* Retrieved 2026-01, from https://geant4.web.cern.ch/documentation/pipelines/master/plg_html/PhysicsListGuide/reference_PL/QBBC.html

Harris, C. R., Millman, K. J., van der Walt, S. J., Gommers, R., Virtanen, P., Cournapeau, D., … Oliphant, T. E. (2020, 9). Array programming with NumPy. *Nature*, *585*(7825), 357–362. Retrieved from https://doi.org/10.1038/s41586-020-2649-2 doi: 10.1038/s41586-020-2649-2

Hartley, D. P., Kletzing, C. A., Santolík, O., Chen, L., & Horne, R. B. (2018). Statistical properties of plasmaspheric hiss from van allen probes observations. *Journal of Geophysical Research: Space Physics*, *123*(4), 2605-2619. Retrieved from https://agupubs.onlinelibrary.wiley.com/doi/abs/10.1002/2017JA024593 doi: https://doi.org/10.1002/2017JA024593

Hubbell, J., & Seltzer, S. (2004). *Tables of x-ray mass attenuation coefficients and mass energy-absorption coefficients (version 1.4).* Online. Gaithersburg, MD: National Institute of Standards and Technology. Retrieved 2025-10, from http://physics.nist.gov/xaamdi doi: https://dx.doi.org/10.18434/T4D01F

Hunter, J. D. (2007). Matplotlib: A 2d graphics environment. *Computing in Science & Engineering*, *9*(3), 90–95. doi: 10.1109/MCSE.2007.55

Lehtinen, N. G., Bell, T. F., & Inan, U. S. (1999). Monte carlo simulation of runaway mev electron breakdown with application to red sprites and terrestrial gamma ray flashes. *Journal of Geophysical Research: Space Physics*, *104*(A11), 24699–24712.

Li, W., Ma, Q., Thorne, R. M., Bortnik, J., Kletzing, C. A., Kurth, W. S., … Nishimura, Y. (2015). Statistical properties of plasmaspheric hiss derived from van allen probes data and their effects on radiation belt electron dynamics. *Journal of Geophysical Research: Space Physics*, *120*(5), 3393-3405. Retrieved from https://agupubs.onlinelibrary.wiley.com/doi/abs/10.1002/2015JA021048 doi: https://doi.org/10.1002/2015JA021048

Lowe, D., Roy, L., Tabocchini, M. A., Rühm, W., Wakeford, R., Woloschak, G. E., & Laurier, D. (2022, Nov 01). Radiation dose rate effects: what is new and what is needed? *Radiation and Environmental Biophysics*, *61*(4), 507-543. Retrieved from https://doi.org/10.1007/s00411-022-00996-0 doi: 10.1007/s00411-022-00996-0

Marshall, R. A., & Bortnik, J. (2018). Pitch angle dependence of energetic electron precipitation: Energy deposition, backscatter, and the bounce loss cone. *Journal of Geophysical Research: Space Physics*, *123*(3), 2412-2423. Retrieved from https://agupubs.onlinelibrary.wiley.com/doi/abs/10.1002/2017JA024873 doi: https://doi.org/10.1002/2017JA024873

McMurchie, E. J. (2022). *Quantifying radiation effects of energetic electron precip-*

itation from the van allen radiation belts into the earth's atmosphere (Unpublished master's thesis). University of Colorado at Boulder.

Mertens, C. J., Meier, M. M., Brown, S., Norman, R. B., & Xu, X. (2013). Nairas aircraft radiation model development, dose climatology, and initial validation. *Space Weather*, *11*(10), 603-635. Retrieved from `https://agupubs.onlinelibrary.wiley.com/doi/abs/10.1002/swe.20100` doi: https://doi.org/10.1002/swe.20100

Niehof, J. T., Morley, S. K., Welling, D. T., & Larsen, B. A. (2022). The spacepy space science package at 12 years. *Frontiers in Astronomy and Space Sciences*, *Volume 9 - 2022*. Retrieved from `https://www.frontiersin.org/journals/astronomy-and-space-sciences/articles/10.3389/fspas.2022.1023612` doi: 10.3389/fspas.2022.1023612

Selesnick, R. S., Tu, W., Yando, K., Millan, R. M., & Redmon, R. J. (2020). Poes/meped angular response functions and the precipitating radiation belt electron flux. *Journal of Geophysical Research: Space Physics*, *125*(9), e2020JA028240. Retrieved from `https://agupubs.onlinelibrary.wiley.com/doi/abs/10.1029/2020JA028240` (e2020JA028240 10.1029/2020JA028240) doi: https://doi.org/10.1029/2020JA028240

Shah, D. J., Sachs, R. K., & Wilson, D. J. (2014, 01). Radiation-induced cancer: a modern view. *British Journal of Radiology*, *85*(1020), e1166-e1173. Retrieved from `https://doi.org/10.1259/bjr/25026140` doi: 10.1259/bjr/25026140

Steven K. Morley, Daniel T. Welling, Josef Koller, Brian A. Larsen, Michael G. Henderson, & Jonathan Niehof. (2010). SpacePy - A Python-based Library of Tools for the Space Sciences. In Stéfan van der Walt & Jarrod Millman (Eds.), *Proceedings of the 9th Python in Science Conference* (p. 67 - 72). doi: 10.25080/Majora-92bf1922-00c

Tobiska, W. K., Bouwer, D., Smart, D., Shea, M., Bailey, J., Didkovsky, L., … Yoon, K. (2016). Global real-time dose measurements using the automated radiation measurements for aerospace safety (armas) system. *Space Weather*, *14*(11), 1053-1080. Retrieved from `https://agupubs.onlinelibrary.wiley.com/doi/abs/10.1002/2016SW001419` doi: https://doi.org/10.1002/2016SW001419

Tobiska, W. K., Didkovsky, L., Judge, K., Weiman, S., Bouwer, D., Bailey, J., … Fuschino, R. (2018). Analytical representations for characterizing the global aviation radiation environment based on model and measurement databases. *Space Weather*, *16*(10), 1523-1538. Retrieved from `https://agupubs.onlinelibrary.wiley.com/doi/abs/10.1029/2018SW001843` doi: https://doi.org/10.1029/2018SW001843

Xu, W., Celestin, S., & Pasko, V. P. (2012). Source altitudes of terrestrial gamma-ray flashes produced by lightning leaders. *Geophysical Research Letters*, *39*(8).

Xu, W., Marshall, R. A., & Tobiska, W. K. (2021). A method for calculating atmospheric radiation produced by relativistic electron precipitation. *Space Weather*, *19*(12), e2021SW002735. Retrieved from `https://agupubs.onlinelibrary.wiley.com/doi/abs/10.1029/2021SW002735` (e2021SW002735 2021SW002735) doi: https://doi.org/10.1029/2021SW002735